6-DoF Full Robotic Calibration based-on 1-D Interferometric Measurements for Micro and Nano-Scales Applications

Houari Bettahar, Olivier Lehmann, Cédric Clevy, Nadège Courjal, Philippe Lutz

▶ **To cite this version:**

Houari Bettahar, Olivier Lehmann, Cédric Clevy, Nadège Courjal, Philippe Lutz. 6-DoF Full Robotic Calibration based-on 1-D Interferometric Measurements for Micro and Nano-Scales Applications. IEEE Transactions on Automation Science and Engineering, 2020, 19 (1), pp.348 - 359. ⟨10.1109/TASE.2020.3031856⟩. ⟨hal-03644504⟩

HAL Id: hal-03644504

https://hal.science/hal-03644504v1

Submitted on 19 Apr 2022

HAL is a multi-disciplinary open access archive for the deposit and dissemination of scientific research documents, whether they are published or not. The documents may come from teaching and research institutions in France or abroad, or from public or private research centers.

L'archive ouverte pluridisciplinaire **HAL**, est destinée au dépôt et à la diffusion de documents scientifiques de niveau recherche, publiés ou non, émanant des établissements d'enseignement et de recherche français ou étrangers, des laboratoires publics ou privés.

HAL Authorization

6-DoF Full Robotic Calibration based-on 1-D Interferometric Measurements for Micro and Nano-Scales Applications

Houari Bettahar, Olivier Lehmann, Cédric Clévy, Nadège Courjal and Philippe Lutz

***Abstract*—This paper proposes an original approach for robotic calibration that is based on measurements along a single direction (1-D). Among all applications, the field of micro and nano robotics has been chosen as case-study because of the strong needs for high positioning accuracy (10-100 nm typically) while measuring with sufficient resolution along multi-DoF (Degrees-of-Freedom) is still a fully open question. 1-D measurements relying on FP (Fabry-Perot) interferences is used and the proposed modelling of a 6-DoF nanopositioning robot enables to derive the measurement strategy as well as the identification procedure for both extrinsic and intrinsic parameters. Experimental investigations demonstrate that the approach is easy to implement, low cost and enables to understand what are the main influential parameters onto positioning accuracy. They also conduct to very high accuracy in 6 DoF positioning: a positioning accuracy estimate of 50 nm and 0.004° has notably been obtained for the full pose (position and orientation respectively) and can be held during several hours after the measurements.**

Note to Practitioners—**The motivation of this work is to give an answer to the growing needs for micro nanopositioning robots having a very high precision for applications in micro-assembly, in the characterization of micro nano components or biological elements, or for minimally invasive surgery. The key contribution of the proposed work relies in the method proposed that enables to efficiently calibrate a serial 6 DoF robot using only 1-D interferometric measurements which overcomes the need for multi DoF, small size, high resolution sensors missing in commercial offers. Moreover, the behavior of such novel robotic solutions is not well known, difficult to model and there is a clear lack of knowledge about main influential parameters. The method proposed in this paper notably enables to achieve the full calibration of the robot (all intrinsic and extrinsic parameters identified) to reach the best positioning accuracy. This first part takes times and the paper shows that it is then possible to adopt a less time taking procedure by only re-identifying extrinsic parameters, and thus to hold these performances over long periods, typically a week.**

***Index Terms*—Micro-Nano Robotics, Nano-positioning, positioning accuracy, robot calibration, Fabry-Perot interferences, optical alignment.**

I. Introduction

Nowadays, positioning accuracy is one of the most important performance criteria in many application fields in order to successfully perform complex tasks. This is all the more true for fastly emerging applications at small scales and/or when robots are required in small free spaces such as micro-assembly [1] [2] [3], manipulation [4] [5] [6], characterization of biological tissues and minimally invasive inspection and surgery [7] [8]... Most of these tasks require to control very accurately the relative position and/or trajectories between a sample (for example, component to handle, tissue or living cell) and a tool used for manipulation or characterization purposes. At small scales, micro and nanopositioning robots are widely used, because of their capability to generate high-resolution motions with high repeatability (typically better than 10 nm for most of commercially available devices). However, positioning accuracy is not well known and difficult to guarantee, because of intrinsic geometric errors accumulations of the built micro-nanopositioning robots, which induces key drawbacks for many applications. This led to develop control laws in closed loop by integrating many sensors, which are complex and costly.

For this sake, research about calibration of micro-nanopositioning robots is getting more and more attention, in order to fulfill high accurate micro-manipulation tasks in many application fields [9] [10] [11].

Works done in [12] targeted to quantify the positioning accuracy of a XYθ serial micro-positioning robot and to identify the main influential parameters after calibration. Experiments show that positioning accuracy can be improved by more than 35 times from 96 μm to 2.5 μm by identifying geometric parameters. However, measurement at the micro-scale is a very challenging issue, especially in 3-D. Micro-scale measurement requires sensing devices with high resolution (e.g., a few nanometers) and accuracy (e.g., tens of nanometers) [13]. State-of-the-art highlights approaches relying on multi-DoF sensing to control micro-nanopositioning robots in multi-DoF but, there is a clear lack of commercially available sensors satisfying multi-DoF measurement and resolution required [14] [15].

In order to overcome the measurement issues, some researchers investigated constrained robot calibration methods, such as point-point position constraint and point-surface position constraint. The constraints in the two approaches can be done either with contact [16] or virtually [17]. Such approaches demonstrate their potential interest for small scale applications, notably [18] proposed a geometric calibration of 6-DoF robot using virtual constraint method in a Scanning Electron Microscope environment. A visual servoing control was used to maintain the object held by the robot in the center

H. Bettahar, O. Lehmann, C. Clévy, N. Courjal, P. Lutz are with FEMTO-ST Institute, Univ. Bourgogne Franche-Comté, UFC/CNRS/ENSMM, 24 rue Savary, 25000 Besançon, France, (e-mails: houari.bettahar@femto-st.fr, olivier.lehmann@femto-st.fr, cclevy@femto-st.fr, philippe.lutz@femto-st.fr, nadege.courjal@femto-st.fr)

of the image. This work reached a positioning accuracy of 10 μm which is still not satisfying enough for most applications at the micro-nano scales. Moreover, only a small volume of the robot's workspace can be explored that can lead to non-observability or poor estimation of some parameters. To eliminate this kind of limitations, several calibration methods based on partial specified pose measurements were raised, leading to other robot calibration methods based on relative position error model [19] [20] or based on relative distance error model [21] [22]. In this latter, the relative distance error of any two poses in robot workspace is applied to calibrate the robot position accuracy [23]. It uses a set of distance measurements either directly achieved by different measurement systems have been used such as mechanical coordinate-measuring machines (CMM)s [24], theodolites [25], laser trackers [21], and ballbars [26]. However, it positioning accuracy relies strangely on the relative distance measurement accuracy and the developed calibration model. Getting accurate measurements remains a key lock, which is not trivial to achieve, notably, at micro-scale.

In this scope, previous works we did for the assembly of micro-optical components, the FP interferometry happening during the active alignment of optical elements is exploited as propreoceptive measurement tool. It demonstrated the high accuracy of this 1-D interferometric measurement principle [27] and the high interest for relative distance-based measurements to achieve the identification of extrinsic parameters [28]. In these works, a positioning accuracy of 390 nm was notably demonstrated for translational motions which is interesting for several applications but still not sufficient for a number of others.

In this paper, the calibration of a 6 DOF robot based on the identification of the extrinsic and intrinsic parameters is addressed. For this sake, a relative distance error calibration model based on 1-D propreoceptive Fabry-Perot measurements has been developed and validated experimentally. This paper is organized as follows. Section II notably explains the FP interferometry principle used for measurements. Section III provides the geometric modelling of the 6-DoF robot while Section IV enables to derive the method for intrinsic and extrinsic parameters identification and Section V the related experimental procedure for parameters identification. Section VI presents the experimental setup and Section VII investigates the performances of the calibrated robot comparing its behavior when the robot is fully calibrated (all intrinsic and extrinsic parameters identified) with when the robot has only its extrinsic parameters identified. Section VIII conclude the paper contribution.

II. 1-D Relative Measurements Based on FP Interferometry

Interferometric sensors are widely used in laboratories as well as in industry fields because of their extremely accurate measurements, high resolution, wide measuring range and bandwidth. These interferometric sensors operate based on different interferometric principles such as Michelson and FP interferences.

Interferences of multiple light beams from the same light source in an optical free-space cavity induces FP interferences as shown in Figure 1. As a result, the light intensity varies periodically with the optical path difference between the beams [29]. Active alignment of a mirror relative to the optical fiber yields FP interferences phenomenon. In this case, the concerned surfaces are the fiber extremity (R_1) in one hand and the mirror surface (R_2) in the other hand. Each time the light comes across one of the surfaces, a portion of it is transmitted out, and the remaining part is reflected back. The net effect is to split a single beam into multiple beams which interfere with each other.

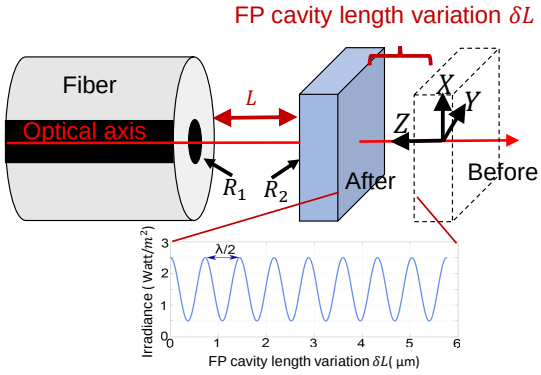

Figure 1. Schematic diagram representing the interferences in a FP optical cavity, with reflected irradiance versus FP cavity length L, at wavelength $\lambda = 1560$ nm .

Based on FP interferences principle, when the reflective surface (R_2) moves along the optical axis (Z-axis), the FP cavity length (L) changes and modifies the reflected light signal accordingly. Therefore, there is a correlation between the FP cavity length L and the interferences figure. A slight variation of the FP cavity length can be identified on the interferences figure.

The periodicity of the irradiance signal directly depends on the wavelength of the laser signal ($\lambda = 1560$ nm). If p is a natural number, the distance between two resonances peaks can be written as in equation 1 (see Figure 1), i.e. the distance variation between two peaks (δL) is a multiple of half wavelength λ of the laser irradiance, such as:

$$\delta L = \frac{\lambda}{2} \cdot p \qquad with \quad p \in \mathbf{N} \tag{1}$$

This FP interferences principle is used in order to achieve 1-D measurements and it is used also for validation after full 6-DoF robot calibration.

For validation, if the mirror is perpendicular to the optical fiber, then the expected displacement of the mirror perpendicular to the optical axis induces no cavity distance variation. Consequently, it induces constant reflected light irradiance versus time. But, if the mirror has a small perpendicularity error with respect to the fiber optical axis, then the expected translation of the mirror perpendicular to the optical axis induces a cavity distance variation δL. Consequently, it generates an oscillating reflected light irradiance at the same time. This principle is used to evaluate positioning accuracy after full

robot calibration. The proposed robotic calibration approach is based on the robot geometric model that is presented in the next section.

III. 6-DoF ROBOT GEOMETRIC MODELING

Geometric model relates the joint and the operational coordinates (coordinates with respect to the world reference frame), by involving robot geometric parameters. Geometric model permits to establish the robot DGM (Direct Geometric Model) and IGM (Inverse Geometric Model), which are successively used to control the robot. These models includes intrinsic parameters that can be identified to calibrate the robot.

Khalil and Kleinfinger representation is one of the most used conventions for the geometric modeling [30]. However, in the case of nearly parallel neighboring axes, the common normal is poorly defined and the calibration is ill-conditioned. For this case, Hayati introduced an extra rotational parameter β_i about the Y_{i-1} axis [31]. Therefore, the modified version by Khalil and Kleinfinger with additional Hayati parameter β_i is used to establish the transformation matrix between two successive links based on two main assumptions: the links are perfectly rigid and the joints are ideal in a sense that there is neither backlash nor elasticity.

For these works, a serial robot is studied because it is of widespread use at small scales. A serial robot is composed of a sequence of n links and n joints where link 0 is the base of the robot and link n is the terminal link. Joint i connects the link i to the link $i-1$. A frame R_i is attached to each link i with [32]:

- The Z_i axis is located along the axis of joint i;
- The X_i axis is located along the common normal between the Z_i and Z_{i+1} axes. If Z_i and Z_{i+1} axes are parallel or collinear, the choice of X_i is not unique: considerations of symmetry or simplicity then allow a rational choice;
- The Y_i axis is located using the right-hand rule to form (X_i, Y_i, Z_i) coordinate system.

The transformation matrix from frame R_{i-1} to frame R_i is expressed using the following four geometric parameters (Figure 2):

- Joint parallelism: β_i is the angle around the axis Y_{i-1} between the axes Z_{i-1} and Z'_{i-1};
- Link twist: α_i is the angle around the axis X'_{i-1} and between the axes Z'_{i-1} and Z_i;
- Link length: d_i is the distance along the axis X'_{i-1} between the axes Z'_{i-1} and Z_i;
- Joint angle:θ_i is the angle around the axis Z_i between the axes X'_{i-1} and X_i;
- Link offset: r_i is the distance along the axis Z_i between the axes X'_{i-1} and X_i.

The variable of the joint i denoted by q_i is θ_i if i is rotational and r_i if i is prismatic. Hence

$$q_i = \theta_i(1-\rho_i) + r_i\rho_i, \tag{2}$$

where

$$\rho_i = \begin{cases} 0, & \text{for rotational joint} \\ 1, & \text{for prismatic joint} \end{cases}. \tag{3}$$

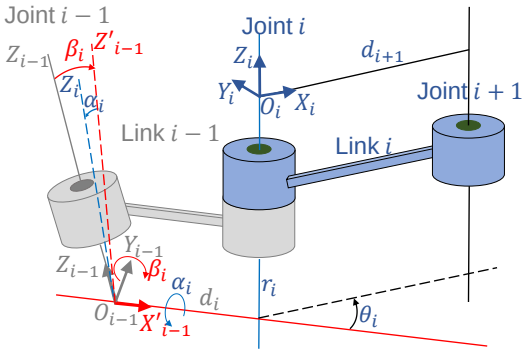

Figure 2. Khalil and Kleinfinger with additional Hayati parameter β_i about Y_{i-1} is used for nearly parallel axes.

Two rotations are required to relate Z_{i-1} to Z_i: a rotation β_i about Y_{i-1} maps Z_{i-1} to Z'_{i-1} and X_{i-1} to X'_{i-1}. Hence, X'_{i-1} axis is located along the common normal between the Z'_{i-1} and Z_i axes. A second rotation α_i about X'_{i-1} maps Z'_{i-1} to Z_i. The angle θ_i is now from X'_{i-1} to X_i about Z_i.

The transformation matrix defining the frame R_i in the frame R_{i-1} is given by

$$^{i-1}T_i = Rot_{Y_{i-1}}(\beta_i).Rot_{X'_{i-1}}(\alpha_i).Trans_{X'_{i-1}}(d_i) .Rot_{Z_i}(\theta_i).Trans_{Z_i}(r_i). \tag{4}$$

The matrices associated with this equation are:

$$Rot_{Y_{i-1}}(\beta_i) = \begin{bmatrix} C\beta_i & 0 & S\beta_i & 0 \\ 0 & 1 & 0 & 0 \\ -S\beta_i & 0 & C\beta_i & 0 \\ 0 & 0 & 0 & 1 \end{bmatrix}; \tag{5}$$

$$Rot_{X'_{i-1}}(\alpha_i) = \begin{bmatrix} 1 & 0 & 0 & 0 \\ 0 & C\alpha_i & -S\alpha_i & 0 \\ 0 & S\alpha_i & C\alpha_i & 0 \\ 0 & 0 & 0 & 1 \end{bmatrix}; \tag{6}$$

$$Trans_{X'_{i-1}}(d_i) = \begin{bmatrix} 1 & 0 & 0 & d_i \\ 0 & 1 & 0 & 0 \\ 0 & 0 & 1 & 0 \\ 0 & 0 & 0 & 1 \end{bmatrix}; \tag{7}$$

$$Rot_{Z_i}(\theta_i) = \begin{bmatrix} C\theta_i & -S\theta_i & 0 & 0 \\ S\theta_i & C\theta_i & 0 & 0 \\ 0 & 0 & 1 & 0 \\ 0 & 0 & 0 & 1 \end{bmatrix}; \tag{8}$$

$$Trans_{Z_i}(r_i) = \begin{bmatrix} 1 & 0 & 0 & 0 \\ 0 & 1 & 0 & 0 \\ 0 & 0 & 1 & r_i \\ 0 & 0 & 0 & 1 \end{bmatrix}, \tag{9}$$

where $C\gamma$ stands for $\cos\gamma$ and $S\gamma$ stands for $\sin\gamma$.

Thus, the general transformation matrix between two frames with consecutive parallel joints becomes:

$$^{i-1}T_i = \begin{bmatrix} A_{11} & A_{12} & A_{13} & A_{14} \\ B_{11} & B_{12} & B_{13} & B_{14} \\ C_{11} & C_{12} & C_{13} & C_{14} \\ 0 & 0 & 0 & 1 \end{bmatrix} \tag{10}$$

where

$$
\begin{aligned}
A_{11} &= C\beta_i C\theta_i + S\alpha_i S\beta_i S\theta_i \\
A_{12} &= S\alpha_i S\beta_i C\theta_i - C\beta_i S\theta_i \\
A_{13} &= C\alpha_i S\beta_i \\
A_{14} &= d_i C\beta_i + r_i C\alpha_i S\beta_i \\
B_{11} &= C\alpha_i S\theta_i \\
B_{12} &= C\alpha_i C\theta_i \\
B_{13} &= -S\alpha_i \\
B_{14} &= -r_i S\alpha_i \\
C_{11} &= S\alpha_i C\beta_i S\theta_i - S\beta_i C\theta_i \\
C_{12} &= S\beta_i C\theta_i + S\alpha_i C\beta_i S\theta_i \\
C_{13} &= C\alpha_i C\beta_i \\
C_{14} &= r_i C\alpha_i C\beta_i - d_i S\beta_i
\end{aligned}
$$

The direct geometric model for a serial-chain manipulator defines the pose (position and orientation) of the end-effector relative to the base given the values of the joint variables and the geometric link parameters. It can be solved by calculating the transformation between the end-effector frames and the base frame. This transformation can be obtained by concatenating the transformations between the frames of the adjacent links:

$$
{}^{0}T_n = {}^{0}T_1 . {}^{1}T_2 \ldots {}^{n-2}T_{n-1} . {}^{n-1}T_n. \tag{12}
$$

The inverse problem is to calculate the joint coordinates corresponding to a given operational coordinates of the end-effector. When exists, the form that gives all the possible solutions (there is rarely a single solution) is the IGM.

The DGM and the IGM are used to control the proposed 6-DoF robot. For this sake, reference frames have been assigned to the 6-DoF robot building stages. For simplification, we choose the same origin for all the frames, which corresponds to the real rotational center of the robot (intersection of joint 4 and 5) when $q_1 = q_2 = q_3 = q_4 = q_5 = q_6 = 0$. The world (base) frame R_w is assigned to be aligned with the first frame when $q_1 = 0$. The assignment of frames is shown in Figure 3, which represents the robot geometric model and the nominal geometrical parameters are given in Table I.

By replacing variables from equation (10) using Table I, The transformation matrix between frame R_i and frame R_{i-1} is given as follows:

$$
{}^{W}T_1 = \begin{bmatrix} 1 & 0 & 0 & 0 \\ 0 & 1 & 0 & 0 \\ 0 & 0 & 1 & q_1 \\ 0 & 0 & 0 & 1 \end{bmatrix}, \quad {}^{1}T_2 = \begin{bmatrix} 0 & 1 & 0 & 0 \\ 0 & 0 & 1 & q_2 \\ 1 & 0 & 0 & 0 \\ 0 & 0 & 0 & 1 \end{bmatrix}
$$

$$
{}^{2}T_3 = \begin{bmatrix} 0 & 1 & 0 & 0 \\ 0 & 0 & 1 & q_3 \\ 1 & 0 & 0 & 0 \\ 0 & 0 & 0 & 1 \end{bmatrix}, {}^{3}T_4 = \begin{bmatrix} Cq_4 & -Sq_4 & 0 & 0 \\ Sq_4 & Cq_4 & 0 & 0 \\ 0 & 0 & 1 & 0 \\ 0 & 0 & 0 & 1 \end{bmatrix},
$$

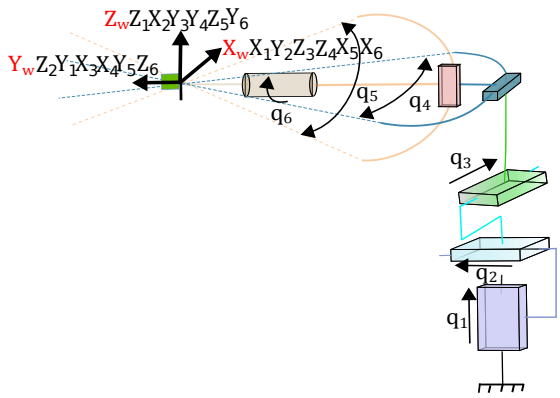

Figure 3. Robot kinematic model.

Table I
NOMINAL PARAMETERS OF ROBOT DIRECT GEOMETRIC MODEL (DGM) FOLLOWING THE HAYATI MODIFIED CONVENTION OF KHALIL AND KLEINFINGER.

Link	ρ_i	β_i	α_i	d_i	θ_i	r_i
1	1	0	0	0	0	q_1
2	1	0	-90	0	-90	q_2
3	1	0	-90	0	-90	q_3
4	0	0	0	0	q_4	0
5	0	0	-90	0	$q_5 - 90$	0
6	0	0	-90	0	q_6	0

$$
{}^{4}T_5 = \begin{bmatrix} Cq_5 & Cq_5 & 0 & 0 \\ 0 & 0 & 1 & 0 \\ Cq_5 & -Sq_5 & 0 & 0 \\ 0 & 0 & 0 & 1 \end{bmatrix},
$$

$$
{}^{5}T_6 = \begin{bmatrix} Cq_6 & -Sq_6 & 0 & 0 \\ 0 & 0 & 1 & 0 \\ -Sq_6 & -Cq_6 & 0 & 0 \\ 0 & 0 & 0 & 1 \end{bmatrix}.
$$

The transformation between the world frame and measurement system frame or the transformation between the end-effector frame and the measurement system frame use the extrinsic geometric parameters. The DGM and the IGM use the intrinsic parameters. A referenced robot control uses extrinsic transformation between world and measurement system frames and the IGM together. Hence, high accurate extrinsic and intrinsic parameters lead to high accurate control of the 6-DoF robot. For this sake, in the next section, the 6-DoF robot extrinsic and intrinsic geometric parameters identification based on a the proposed robotic approach is presented.

IV. 6-DoF ROBOT EXTRINSIC AND INTRINSIC GEOMETRIC PARAMETERS IDENTIFICATION

In order to achieve the full robot geometric calibration (both intrinsic and extrinsic parameters) based on relative distance measure in 1-D, a new calibration model is proposed. The distance measure is achieved based on very high accurate FP

interferometric principle measurements as presented in section II. In order to develop the geometrical model of the robot, the main reference frames are defined as schematically shown in Figure 4. R_f is assigned to the fiber frame, its origin, labeled O_f, is defined as the intersection point between the optical axis and the outer surface of the fiber. R_e corresponds to the robot end-effector frame, its origin, labeled O_e, corresponds to the real rotational center of the robot (intersection of joint 4 and 5). The $\overrightarrow{O_eX_e}$, $\overrightarrow{O_eY_e}$ and $\overrightarrow{O_eZ_e}$ are the expected motion directions of the robot, where $R_e = R_6$. R_t corresponds to the tool frame, its origin, labeled O_t, is defined as the intersection between the $\overrightarrow{O_eZ_e}$ and the mirror plane ($Y_tO_tX_t$). R_w is assigned to the world frame, its origin, labeled O_w, corresponds to the real rotational center of the robot (intersection of joint 4 and 5) when all axes are at zero (initial configuration), with the same directions as the first stage axes R_1.

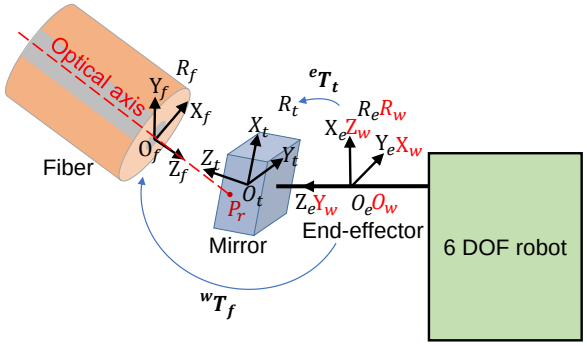

Figure 4. The robotic positioning scheme with frames assignment.

The vector $\overrightarrow{O_eZ_e}$ is assumed to be collinear with the vector $\overrightarrow{O_wY_w}$. Thus, the homogeneous transformation matrix from the world frame to the fiber frame is given in equation (13), and the transformation matrix from the end-effector frame to the tool frame is given in equation (14).

$$
\begin{aligned}
&{}^{w}T_f = Trans_{X_w}(x_{wf}).Trans_{Y_w}(y_{wf}).Trans_{Z_w}(z_{wf}) \\
&.Rot_{X_w}(\beta_{wf}).Rot_{Z_w}(\theta_{wf}) = \\
&\begin{bmatrix} C\theta_{wf} & -S\theta_{wf} & 0 & x_{wf} \\ C\beta_{wf}S\theta_{wf} & C\theta_{wf}C\beta_{wf} & -S\beta_{wf} & y_{wf} \\ S\beta_{wf}S\theta_{wf} & C\theta_{wf}S\beta_{wf} & C\beta_{wf} & z_{wf} \\ 0 & 0 & 0 & 1 \end{bmatrix}
\end{aligned} \tag{13}
$$

where x_{wf}, y_{wf} and z_{wf} are the translational coordinates of the origin of the fiber frame O_f with respect to the world frame, along X_w, Y_w and Z_w axis respectively. β_{wf} is the angle between Y_f and Z_w around X_w axis and θ_{wf} is the angle between X_f and X_w around Z_w axis.

$$
\begin{aligned}
&{}^{e}T_t = Trans_{Z_e}(Z_{et}).Rot_{X_e}(\beta_{et}).Rot_{Y_e}(\theta_{et}) = \\
&\begin{bmatrix} C\theta_{et} & 0 & S\theta_{et} & 0 \\ S\theta_{et}S\beta_{et} & C\beta_{et} & -C\theta_{et}S\beta_{et} & 0 \\ -C\beta_{et}S\theta_{et} & S\beta_{et} & C\theta_{et}C\beta_{et} & Z_{et} \\ 0 & 0 & 0 & 1 \end{bmatrix}
\end{aligned} \tag{14}
$$

where Z_{et} is the translational coordinate of the origin of the mirror O_t with respect to the end-effector frame, along Z_e axis. β_{et} and θ_{et} are the rotational coordinates of X_t and Y_t axes of the mirror with respect to the end-effector frame, around the X_e and Y_e respectively.

P_r is the reflection point projection of the laser spot on the mirror plane ($Y_tO_tX_t$). ${}^{w}P_r({}^{w}P_{rx}, {}^{w}P_{ry}, {}^{w}P_{rz})$ is the reflection point projection in the world frame R_w. ${}^{t}P_r({}^{t}P_{rx}, {}^{t}P_{ry}, 0)$ is the reflection point in the tool frame R_t.

The proposed extrinsic and intrinsic parameters identification uses the optical axis 3-D parametric equation and the plane equation of the mirror.

The 3-dimensional parametric form of the equation of optical axis line is defined by a point on the optical axis line O_f and its direction vector $\overrightarrow{Z_f}$. The point O_f (x_{wf}, y_{wf}, z_{wf}) is a point with respect to the world frame R_w through which the optical axis line passes. The unit vector $\overrightarrow{Z_f}$ (a_{wf}, b_{wf}, c_{wf}) is the direction vector of the optical axis line with respect to the world frame R_w. Therefore, the 3-dimensional parametric equations of the line carrying the vector $\overrightarrow{O_fZ_f}$ (optical axis) can be written as follows:

$$
\begin{cases} x = a_{wf}L + x_{wf} \\ y = b_{wf}L + y_{wf} \\ z = c_{wf}L + z_{wf} \end{cases}, \tag{15}
$$

where $\sqrt{a_{wf}^2 + b_{wf}^2 + c_{wf}^2} = 1$.

The intersection point between the mirror plane ($Y_tO_tX_t$) and the line carries the vector $\overrightarrow{O_eZ_e}$ is O_t (x_{wt}, y_{wt}, z_{wt}). The mirror plane is defined by the point O_t (x_{wt}, y_{wt}, z_{wt}) in the plane with respect to the world frame and the normal unit vector to the plane $\overrightarrow{Z_t}$ (a_{wt}, b_{wt}, c_{wt}). If $M(x, y, z)$ is any other point which belongs to the mirror plane, then the equation of the mirror plane can be written as follows:

$$
\overrightarrow{O_tM} \cdot \overrightarrow{O_tZ_t} = 0. \tag{16}
$$

This yields:

$$
a_{wt}(x - x_{wt}) + b_{wt}(y - y_{wt}) + c_{wt}(z - z_{wt}) = 0. \tag{17}
$$

By considering $d_{wt} = -a_{wt}x_{wt} - b_{wt}y_{wt} - c_{wt}z_{wt}$, then:

$$
a_{wt}x + b_{wt}y + c_{wt}z + d_{wt} = 0, \tag{18}
$$

where: $\sqrt{a_{wt}^2 + b_{wt}^2 + c_{wt}^2} = 1$.

From the other hand, the columns of a rotation matrix are orthogonal unit vectors along X, Y and Z axes respectively. Hence, the third column of a rotation matrix represents the unit vector along Z-axis. Accordingly, the transformation matrix ${}^{w}T_t$ of the tool frame in the world frame can be written using the unit vector $\vec{Z}_t(a_{wt}, b_{wt}, c_{wt})$ with respect to the world frame as follows:

$$
\begin{aligned}
&{}^{w}T_t(q, \epsilon, \beta_{et}, \theta_{et}, Z_{et}) = {}^{w}T_e(q, \epsilon).{}^{e}T_t(\beta_{et}, \theta_{et}, Z_{et}) = \\
&\begin{bmatrix} r & r & a_{wt} & x_{wt} \\ r & r & b_{wt} & y_{wt} \\ r & r & c_{wt} & z_{wt} \\ 0 & 0 & 0 & 1 \end{bmatrix}
\end{aligned} \tag{19}
$$

The label r is appointed to the matrix elements that are not required in the development of our approach.

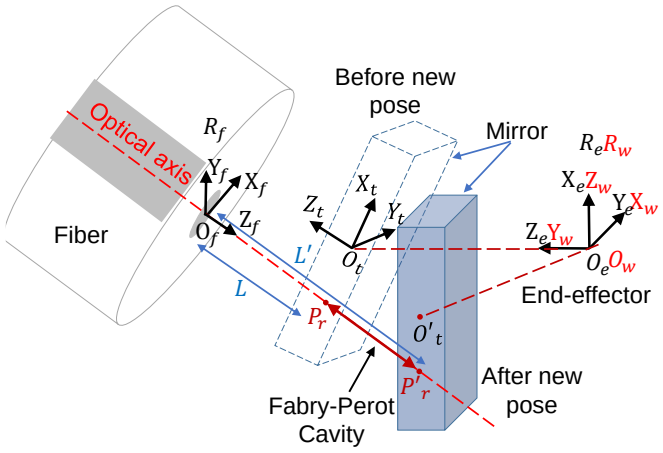

Figure 5. Mirror before the new pose and after the new pose.

${}^{w}T_{e}$ is Direct Geometric Model (DGM), ϵ is the vector of the real (unknown intrinsic) parameters of the geometric errors, and q is the joint coordinates vector.

From the other side, the mirror plane equation given in equation (18), can be deduced from the transformation matrix between the world frame and the tool (mirror) frame given in equation. (19), where:

$a_{wt} = {}^{w}T_t(1,3)$, $b_{wt} = {}^{w}T_t(2,3)$, $c_{wt} = {}^{w}T_t(3,3)$, $x_{wt} = {}^{w}T_t(1,4)$, $y_{wt} = {}^{w}T_t(2,4)$, $z_{wt} = {}^{w}T_t(3,4)$.

The direction vector $\overrightarrow{Z_t}$ (a_{wt},b_{wt}, c_{wt}) is orthogonal to the mirror plane and passes through the origin O_t (x_{wt},y_{wt}, z_{wt}) of the tool frame (mirror frame).

The new mirror plane equation after new pose with respect to the world frame is given as follows:

$$a'_{wt}x + b'_{wt}y + c'_{wt}z + d'_{wt} = 0, \tag{20}$$

where $a'_{wt}, b'_{wt}, c'_{wt}$ and d'_{wt} are the coefficients of the mirror plane equation after the new pose.

As shown in Figure 5, the fiber is fixed, which means that the optical axis equation stays unchanged. From the other side, displacing the mirror from one pose to another yields two plane equations (before and after the new pose).

The mirror plane equations before and after the new pose are given as follows:

$$\begin{cases} a_{wt}x + b_{wt}y + c_{wt}z + d_{wt} = 0 \\ a'_{wt}x + b'_{wt}y + c'_{wt}z + d'_{wt} = 0 \end{cases}. \tag{21}$$

Using the optical axis line equation given in equation (15). The intersection of the optical axis line with the mirror plane before the new pose gives:

$$a_{wt}(a_{wf}L+x_{wf})+b_{wt}(b_{wf}L+y_{wf})+c_{wt}(c_{wf}L+z_{wf})+d_{wt} = 0. \tag{22}$$

The intersection of the optical axis line with the mirror plane after the new pose gives:

$$a'_{wt}(a_{wf}L'+x_{wf})+b'_{wt}(b_{wf}L'+y_{wf})+c'_{wt}(c_{wf}L'+z_{wf})+d'_{wt} = 0. \tag{23}$$

Then, L and L' can be calculated respectively as follow:

$$L = \frac{-(a_{wt}x_{wf} + b_{wt}y_{wf} + c_{wt}z_{wf} + d_{wt})}{a_{wt}a_{wf} + b_{wt}b_{wf} + c_{wt}c_{wf}}, \tag{24}$$

$$L' = \frac{-(a'_{wt}x_{wf} + b'_{wt}y_{wf} + c'_{wt}z_{wf} + d'_{wt})}{a'_{wt}a_{wf} + b'_{wt}b_{wf} + c'_{wt}c_{wf}}. \tag{25}$$

The mirror displacement along the optical axis after the new pose can be deduced as follows:

$$dL = L' - L = \frac{(a_{wL}x_{wf} + b_{wL}y_{wf} + c_{wL}z_{wf} + d_{wt})}{a_{wt}a_{wf} + b_{wt}b_{wf} + c_{wt}c_{wf}} - \frac{(a'_{wt}x_{wf} + b'_{wt}y_{wf} + c'_{wt}z_{wf} + d'_{wt})}{a'_{wt}a_{wf} + b'_{wt}b_{wf} + c'_{wt}c_{wf}}, \tag{26}$$

where:

$d_{wt} = -a_{wt}.\ {}^{w}T_t(1,4) - b_{wt}.\ {}^{w}T_t(2,4) - c_{wt}.\ {}^{w}T_t(3,4)$,
$a'_{wt} = {}^{w}T'_t(1,3)$, $b'_{wt} = {}^{w}T'_t(2,3)$, $c'_{wt} = {}^{w}T'_t(3,3)$,
$d'_{wt} = -a'_{wt}.\ {}^{w}T'_t(1,4) - b'_{wt}.\ {}^{w}T'_t(2,4) - c'_{wt}.\ {}^{w}T'_t(3,4)$.

And at the same time, this mirror displacement along the optical axis after the new pose is measured from the FP interferometric measurements. This displacement dL, can be written as a function of robot intrinsic and extrinsic geometric parameters as follows:

$$dL = f(q, \epsilon, \theta_{et}, \beta_{et}, a_{wf}, b_{wf}, c_{wf}, x_{wf}, y_{wf}, z_{wf}, Z_{et}). \tag{27}$$

Equation 27 represents the model for extrinsic and intrinsic parameters identification. Displacing the mirror in different poses using the 6 DoF robot, will lead to form a system of non-linear equations, where the unknowns are the intrinsic and the extrinsic geometric parameters. The system of equations can be solved using different optimization algorithms (it is detailed in the next section).

When the intrinsic and the extrinsic parameters of the robot are identified, the point of intersection between the optical axis and the plane of the mirror with respect to the world frame can be deduced by calculating the distance L between the mirror and the fiber using equation (24) and then calculating the Cartesian coordinates of the reflection point ${}^{w}P_r({}^{w}P_{rx}, {}^{w}P_{ry}, {}^{w}P_{rz})$ in the world frame using the following equation:

$$\begin{cases} {}^{w}P_{rx} = a_{wf}L + x_{wf} \\ {}^{w}P_{ry} = b_{wf}L + y_{wf} \\ {}^{w}P_{rz} = c_{wf}L + z_{wf} \end{cases}. \tag{28}$$

At the initial mirror pose ($q_1 = q_2 = q_3 = q_3 = q_4 = q_5 = q_6 = 0$), the Direct Geometric Model (DGM) transformation matrix is written as a function of intrinsic parameters errors ${}^{w}T_e(q = 0, \epsilon)$.

By replacing the already deduced vector ${}^{w}P_r$ and the transformation matrices ${}^{e}T_t$ and ${}^{w}T_e$, the vector ${}^{t}P_r$ can be deduced as follows:

$${}^{t}P_r = {}^{e}T_t^{-1}.\ {}^{w}T_e^{-1}.\ {}^{w}P_r. \tag{29}$$

After having developed the robotic model for extrinsic and intrinsic parameters identification, this model combines 6-DoF robot motion with a high accurate 1-D FP measurements in order to identify the extrinsic and the intrinsic parameters of the robot. In order to detail the robotic calibration approach, the next section presents the experimental procedure for robot extrinsic and intrinsic parameters identification.

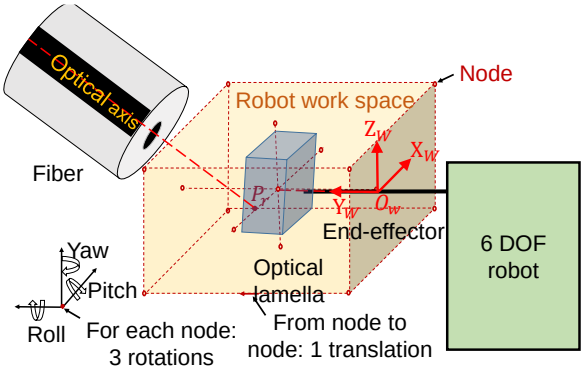

Figure 6. Measurement strategy for robot calibration.

V. Experimental procedure of robot extrinsic and intrinsic parameters calibration

The whole procedure of the full robot calibration (both intrinsic and extrinsic parameters identified) includes measurement, identification, parameters correction and validation step.

A. Measurement strategy

In order to cover all the robot workspace and to achieve a high accurate measurement. The proposed measurement strategy consists of 2 steps:

- The mirror held on the robot was put in a cubical workspace with 15 nodes is chosen as shown in Figure 6. For each node, three continuous rotations of the mirror are applied, around X_w, Y_w, Z_w. Rotation of $[-3°\ \ 3°]$ is applied around X_w and Y_w, and $[0°\ \ 90°]$ around Z_w with angular velocity control. Each rotation around an axis enables to obtain one equation. Hence, for each node 3 equations are obtained, which means for 15 nodes 45 equations can be obtained;
- Different mirror orientations are given. By choosing two angular values for each rotation, $Rot_{X_w}(q_4 = (0°, 3°))$, $Rot_{Z_w}(q_5 = (0°, 3°))$ and $Rot_{Y_w}(q_6 = (0°, 90°))$, 2^3 angular combinations are obtained. For each angular combination (each orientation), three translations are applied along X_w, Y_w and Z_w (3 equations), thus yields 24 equations. Translation of $[-150\ \ +150]\ \mu m$ is applied along X_w and Z_w and $[-20\ \ +20]\ \mu m$ along Y_w with translational velocity control. Wavelength scan distance measure is used based on FP interferometry before and after each translation along X_w and Z_w axes in order to determine the sign of dL.

The two previous measurement steps can give 69 equations. This non-linear minimization problem can be solved using various algorithms. The Levenberg-Marquardt method is most often cited and used in the literature. Such a method makes a compromise between the gradient method (launch of the algorithm far from the minimum) and Newton's method (neighborhood of the solution, acceleration of convergence). In addition, such a method frees itself from the problems of singularities of the Hessian matrix. Levenberg-Marquardt method is used for the identification of the robot extrinsic and intrinsic parameters.

B. 6-DoF Nanopositioning robot control after full calibration

The 6-DoF Nanopositioning robot control after full calibration is shown in the scheme in Figure 7. The control scheme of the robot uses the identified extrinsic and intrinsic parameters of the robot. The inverse kinematic model of the robot is calculated based on the identified intrinsic parameters of the robot. The two transformation matrices between the end-effector and the tool and then between the tool and the reflection spot P_r are calculated based on the identified extrinsic parameters.

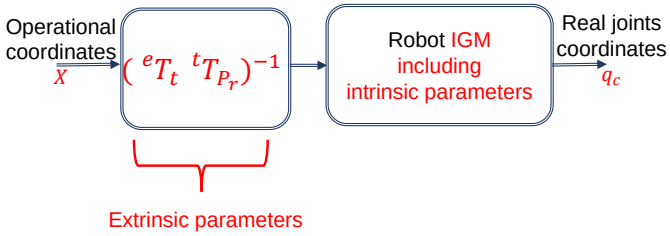

Figure 7. 6-DoF Nanopositioning robot control after full calibration.

The experimental setup used to validate the proposed calibration approach is presented in the next section.

VI. Experimental setup

The proposed experimental setup for 6-DoF robotic calibration based on 1-D interferometric measurements is shown in Figure 8. The mirror is held by a 6-DoF serial robot to control its poses. The fiber ferrule is held by an other XYZ manual positioner which is fixed in front of the 6-DoF robot, it is used to pre-position the fiber ferrule.

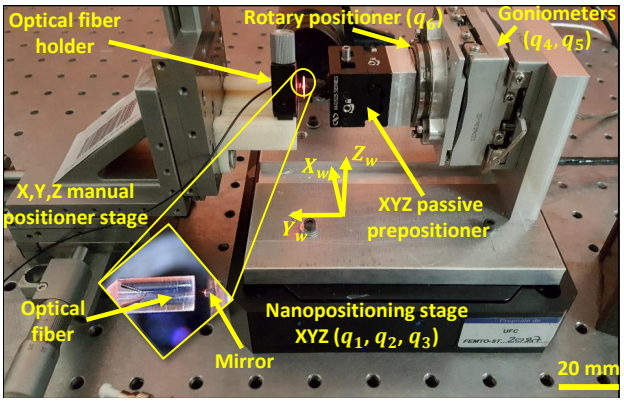

Figure 8. Robotic experimental platform.

The experimental setup is placed on an anti-vibration table. The 6-DoF robot is assembled with minimum geometric errors based on one (XYZ) nanopositioning stage followed by a bracket support, which is fabricated specifically to join the (XYZ) translation stage (q_1, q_2, q_3) to a set of two gomiometers (q_4, q_5) and then a rotary positioner (q_6) (see Figure 8). The two gomiometers are used for rotation around X_w-axis and Z_w-axis and the rotary positioner for rotation around Y_w-axis. A XYZ prepositioner is placed after the rotary positioner

for coarse adjustment of the rotation center of the whole assembled 6-DoF robot.

The (XYZ) nanopositioning stage is a PIMars P-563.3CD, its resolution is $0.5\ nm$. It is controlled via a E-712 controller. The two goniometers are SGO-60.5 and SGO-77.5, their resolution is $0.57\ \mu°$. They use the stick-slip principle and are controlled by MCS-3D unit. The SGO-60.5 goniometer's center of rotation is 60.5 mm. The SGO-77.5 goniometer's center of rotation is extended to 77.5 mm. The rotary positioner is SR-3610-S, its resolution is $1.1\ \mu°$. It uses the piezo principle and is controlled by MCS-3D unit. E-712 controller and MCS-3D unit are controlled via Matlab.

The optical fiber is connected to an optical set up. This optical setup consists in a laser light source (wavelength $\lambda = 1560\ n$m). This latter is connected to a circulator and then to the fiber ferrule. The reflected optical irradiance from mirror through the fiber ferrule is the feedback information for the 6-DoF robot control loop.
This set up enables the acquisition of the reflected optical irradiance signal from the mirror surface, coming back through the fiber ferrule and then through the beam circulator.

The next section studies the optical performances after robot extrinsic and intrinsic parameters identification.

VII. Experimental results

A. Performances after full 6-DoF robot calibration

Figure 9 represents the optical irradiance during a rotation q_6 around Z_6 axis before calibration. Figure 10 represents the optical irradiance during a circular translation on the mirror plane before calibration. The fringes (peaks) on the optical irradiance are due to FP cavity variation along the optical axis. This proves the strong influence of geometric errors, that can be extrinsic and/or intrinsic.

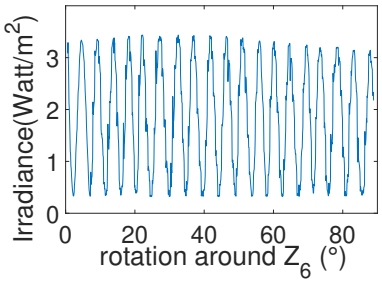

Figure 9. Optical signal (irradiance) when a rotation q_6 around Z_6 axis is done before calibration.

The robot calibration aims to reach a 6-DoF positioning that does not induce a FP cavity variation along the optical axis i.e, applying rotations and translations along the mirror plane without inducing a distance change along the optical axis (the reflection point on the mirror plane is kept fixed).

The method presented in previous sections conducts to identify both intrinsic and extrinsic parameters whose identified values are provided in Table II and Table III respectively. Figure 11 represents the obtained results after identification of both extrinsic and intrinsic parameters of the 6-DoF robot for 3 rotations around Z_f, for the reflection point projection on the mirror $P_r(141.1, 116.34)$, calculated from equation (29).

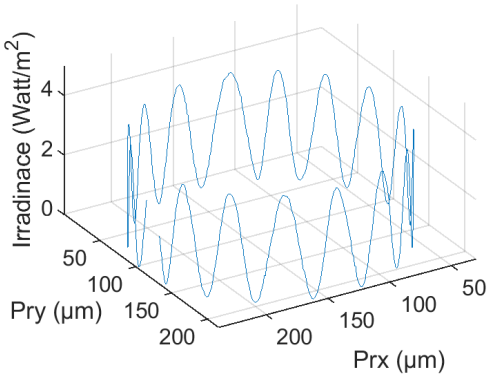

Figure 10. Circular translation on the mirror plane before calibration.

Table II
Identified robot intrinsic parameters.

Link	ρ_i	$\beta_i(°)$	$\alpha_i(°)$	d_i (μm)	$\theta_i(°)$	r_i (μm)
1	1	0	0	0	0	q_1
2	1	0	-90.13	0	-89.22	q_2
3	1	0	-90.29	0	-89.47	q_3
4	0	-0.26	0.25	-4.20	$q_4 - 0.07$	0
5	0	0	-89.45	-2.21	$q_5 - 90.49$	0
6	0	0	-90.57	0	$q_6 + 0.14$	0

For rotations around Z_f, the corresponding optical irradiance, the 3 translational joints and the 2 rotational joints (joint 4 and 5) are plotted.

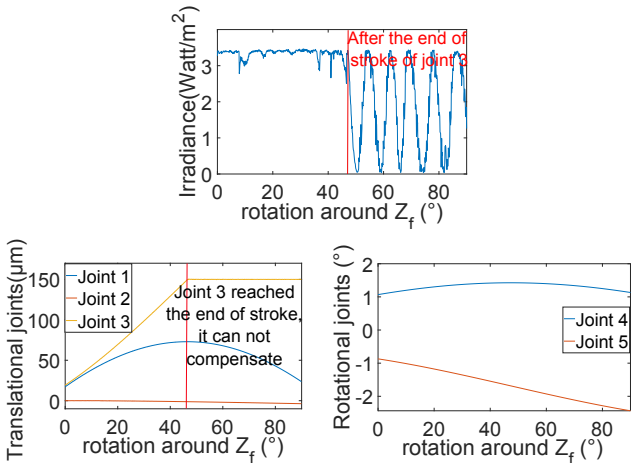

Figure 11. Rotation q_6 around Z_f axes in operational coordinates when the reflection point projection is in $P_r(141.1, 116.34)$, after robot extrinsic and intrinsic parameters identification.

Results show that, after full robot calibration, the joints intervene in order to move the rotation center of the robot to the reflection point of the laser spot P_r and maintains it at that point (reflection point P_r) during rotations in operational coordinates. For example, for a rotation q_6 around Z_f, the translational and rotational joints intervene in order

Table III
IDENTIFIED EXTRINSIC PARAMETERS.

Parameters	β_{et}	θ_{et}	β_{wf}	θ_{wf}	Z_{et}	x_{wf}	y_{wf}	z_{wf}	${}^{w}P_{rx}$	${}^{w}P_{ry}$	${}^{w}P_{rz}$
Values	$0.768°$	$-0.613°$	$0.721°$	$-0.533°$	$1.61\ \mu$m	$113.40\ \mu$m	$916.1\ \mu$m	$115.3\ \mu$m	$155.5\ \mu$m	$-3.82\ \mu$m	$-109.78\ \mu$m

to maintain the rotation at the reflection point P_r, where the optical irradiance is constant until the saturation of at least one translational joint, the frequency of the fringes (peaks) increase, which represents an increase in FP cavity variation during the rotation.

Figure 12 shows the optical irradiance corresponding to a circular translation along the optical fiber plane before calibration, after extrinsic parameters identification, and after extrinsic and intrinsic parameters identification. Results shows many fringes on the optical signal before calibration. After only extrinsic parameters identification, there is still almost half of FP peak. After extrinsic and intrinsic parameters identification, the irradiance is constant and it is maximum compared with the two others cases. It is also important to note that the maximum irradiance obtained is largely improved when the positioning robot is calibrated. This demonstrates that there is no FP cavity variation during the circular translation along the optical fiber plane.

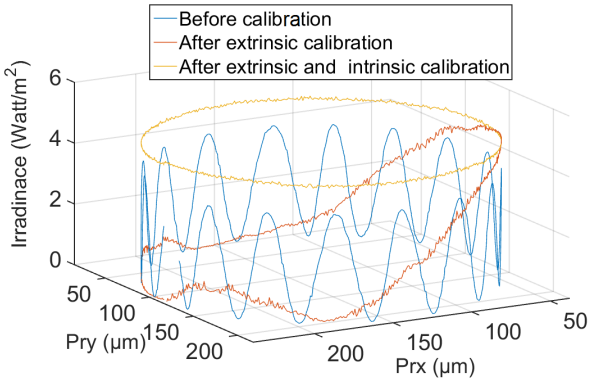

Figure 12. The optical irradiance corresponding to a circular translation on the mirror plane before robot calibration, after robot extrinsic parameters calibration and after robot extrinsic and intrinsic parameters calibration.

B. Full calibration durability and parameters behavior investigation

At micro-scale and more generally in precision robotics, drift often happens. For this reason, the durability of the obtained performances needs to be studied. In order to evaluate the durability of the calibrated extrinsic and intrinsic parameters of the 6-DoF robot, a circular translation along the optical fiber plane is applied every 2 hours for 14 hours after the end of the full calibration (which defines time "T_0").

Figure 13 shows the obtained optical irradiance for each circular translation along the optical fiber plane for each

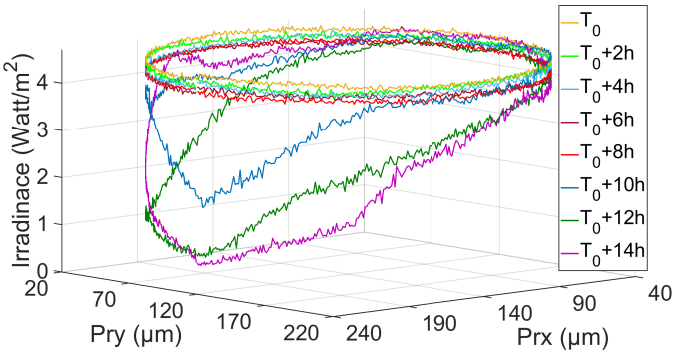

Figure 13. Durability evaluation of the fully calibrated robot (both extrinsic and intrinsic parameters) by applying circular translation on the optical fiber plane every 2 hours without recalibration for 14 hours after the end of the full calibration (the full calibration ends at time T_0).

Table IV
IDENTIFIED EXTRINSIC PARAMETERS AFTER, 1, 2, 7 AND 8 DAYS FROM THE FIRST FULL ROBOT CALIBRATION.

Parameters	After 1 day	After 2 days	After 7 days	After 8 days
β_{et}	$0.781°$	$0.785°$	$0.802°$	$0.811°$
θ_{et}	$-0.615°$	$-0.619°$	$-0.710°$	$-0.702°$
β_{wf}	$0.729°$	$0.725°$	$0.784°$	$0.763°$
θ_{wf}	$-0.561°$	$-0.565°$	$-0.591°$	$-0.561°$
Z_{et}	$1.42\ \mu$m	$1.52\ \mu$m	$2.1\ \mu$m	$2.3\ \mu$m
x_{wf}	$112.9\ \mu$m	$112.3\ \mu$m	$112.4\ \mu$m	$113.3\ \mu$m
y_{wf}	$917.2\ \mu$m	$917.8\ \mu$m	$920\ \mu$m	$918.8\ \mu$m
z_{wf}	$115.7\ \mu$m	$116.4\ \mu$m	$113.1\ \mu$m	$112.2\ \mu$m
${}^{w}P_{rx}$	$154.8\ \mu$m	$154.4\ \mu$m	$149.2\ \mu$m	$148.7\ \mu$m
${}^{w}P_{ry}$	$-3.75\ \mu$m	$-3.61\ \mu$m	$-3.4\ \mu$m	$-3.54\ \mu$m
${}^{w}P_{rz}$	$-109.08\ \mu$m	$-109.87\ \mu$m	$-106.54\ \mu$m	$-107.53\ \mu$m

2 hours from the end of the full (extrinsic and intrinsic) calibration at T_0. The optical irradiance remains constant during the 8 first hours and it starts to derive after 10 hours and then it derives increasingly after 12 and 14 hours.

In order to study the parameters changes to drifts, two robot extrinsic and intrinsic parameters identifications are repeated (the sequence of all experiments done is detailed in Fig. 16). The first one is done one day after the first full robot calibration, and the obtained identified extrinsic and intrinsic

Table V
IDENTIFIED ROBOT INTRINSIC PARAMETERS, ONE DAY AFTER THE FIRST FULL ROBOT CALIBRATION.

Link	ρ_i	$\beta_i(°)$	$\alpha_i(°)$	d_i (μm)	$\theta_i(°)$	r_i (μm)
1	1	0	0	0	0	q_1
2	1	0	-90.13	0	-89.22	q_2
3	1	0	-90.29	0	-89.47	q_3
4	0	-0.29	0.25	-4.2	$q_4 - 0.07$	0
5	0	0	-89.45	-2.21	$q_5 - 90.49$	0
6	0	0	-90.57	0	$q_6 + 0.16$	0

Table VI
IDENTIFIED ROBOT INTRINSIC PARAMETERS, TWO DAYS AFTER THE FIRST FULL ROBOT CALIBRATION.

Link	ρ_i	$\beta_i(°)$	$\alpha_i(°)$	d_i (μm)	$\theta_i(°)$	r_i (μm)
1	1	0	0	0	0	q_1
2	1	0	-90.13	0	-89.22	q_2
3	1	0	-90.29	0	-89.47	q_3
4	0	-0.30	0.25	-4.2	$q_4 - 0.07$	0
5	0	0	-89.45	-2.21	$q_5 - 90.49$	0
6	0	0	-90.57	0	$q_6 +$ 0.17	0

Table VII
IDENTIFIED INTRINSIC PARAMETERS AFTER 8 DAYS FROM THE FIRST FULL ROBOT CALIBRATION.

Link	ρ_i	$\beta_i(°)$	$\alpha_i(°)$	d_i (μm)	$\theta_i(°)$	r_i (μm)
1	1	0	0	0	0	q_1
2	1	0	-90.13	0	-89.22	q_2
3	1	0	-90.29	0	-89.47	q_3
4	0	-0.42	0.29	-4.2	$q_4 - 0.07$	0
5	0	0	-89.38	-2.21	$q_5 - 90.49$	0
6	0	0	-90.57	0	$q_6 +$ 0.19	0

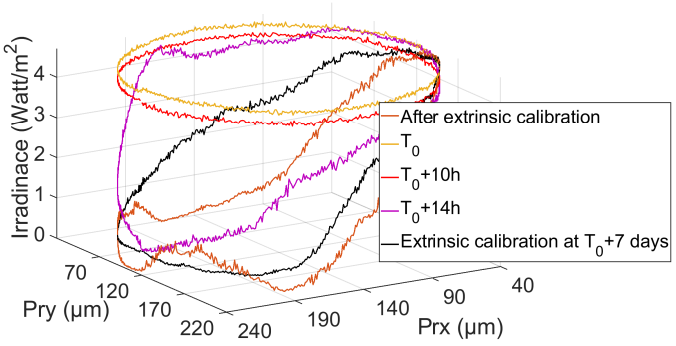

Figure 14. The obtained optical irradiance for circular translation on the optical lamella plane for only robot extrinsic parameters calibration, after 7 days from the first full calibration.

parameters are shown in column one of Table IV and Table V respectively. The second one is done two days after the full calibration and the obtained identified extrinsic and intrinsic parameters are shown in column two of Table IV and Table VI respectively. From the obtained identified parameters, all robot extrinsic parameters change from one day to another and only one intrinsic parameter that changes, which is β_4. θ_6 is dependent to θ_{et}, therefore it can be fixed.

After 7 days from the first full robot calibration, only robot extrinsic parameters calibration is done, the obtained identified extrinsic parameters are shown in column three of Table IV. The obtained optical irradiance which corresponds to the circular translation along the optical lamella plane is highlighted in red color in Figure 14.

The obtained optical irradiance which corresponds to the circular translation along the mirror plane is not maximum and is not constant, which means that there is small FP cavity variation. Hence, we can conclude that during the 7 days, some intrinsic parameters were slightly changing. In order to verify that some intrinsic parameters are changing, a full extrinsic and intrinsic robot parameters is identified one day after (8 days from the first full robot calibration). The obtained identified extrinsic and intrinsic parameters are given in column four of Table IV and Table VII respectively and shows that some intrinsic parameters are changing slowly with time.

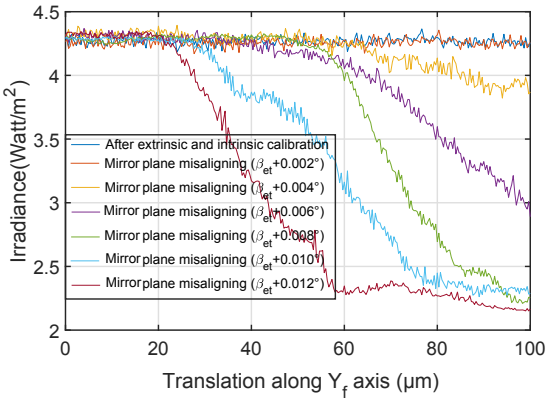

Figure 15. Experimental estimation of angular accuracy when a small compensation error of β_{et} parameter is created.

Figure 16 summarize the experimental protocol for full calibration durability and parameters behavior investigation.

In order to estimate the positioning accuracy, after identification of both intrinsic and extrinsic parameters, a translation along Y_f axis (parallel to the plane of the fiber) is applied after having modified the identified parameter β_{et} by adding each time $0.002°$ (misaligning the mirror from the fiber plane). $(\beta_{et})_{set} = (\beta_{et})_{identified} + \varepsilon$, such that $0.002° \leq \varepsilon \leq 0.012°$. The obtained optical irradiance for each translation is shown in Figure 15 and highlights that the optical irradiance starts to derive after having modified β_{et} by $0.004°$, which is an estimate of the rotational positioning accuracy. The same optical irradiance can be estimated to $1/8$ of half oscillation period, which corresponds approximately to a translational positioning accuracy estimate of $50\ nm$.

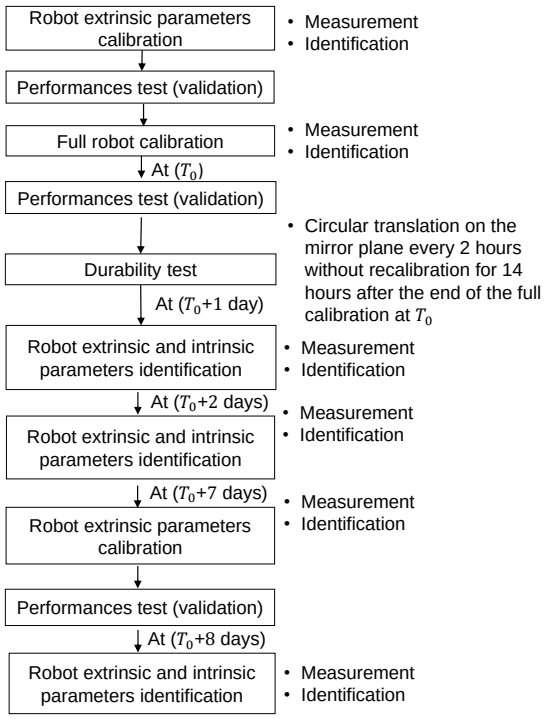

Figure 16. Flowchart of the experimental protocol for full calibration durability and parameters behavior investigation.

In summary, full (extrinsic and intrinsic parameters) robot calibration can be maintained for about 8 hours, without parameters change. Optical irradiance derivation starts after 10 hours. All robot extrinsic parameters change from one day to another and only one intrinsic parameter that changes, which is β_4. Therefore, the optical irradiance derivation is because of extrinsic geometric parameters change. Doing extrinsic parameters calibration after 7 days from full parameters calibration demonstrates that intrinsic parameters were changing slowly with time.

VIII. Conclusion

Positioning accuracy is one of the most important performance criteria ore especially for nanopositioning robots. However, there are many extrinsic and intrinsic parameters that induce inaccuracy. In this paper, these extrinsic and intrinsic parameters were identified to calibrate the nanopositioning robot studied, in order to improve its positioning accuracy.

A robotic approach was proposed for 6-DoF nanopositioning robot calibration. This approach uses 1-D relative distance measurements in order to identify extrinsic and intrinsic geometric parameters, through a new reliable robotic calibration model and a dedicated measurement strategy for high measurement accuracy. The 1-D relative distance measurements is based on 1-D FP interferometric measurements.

After full 6-DoF robot calibration, no FP fringes appear on the optical irradiance for rotations around X_f, Y_f and Z_f axes, neither for circular translation along the mirror plane. A translational and rotational positioning accuracy estimate of about 50 nm and 0.004° have been obtained respectively. Moreover works shown that this level of performances can be held during several hours.

The alignment of the mirror with respect to the fiber is easily reachable after full robot calibration. Moreover, two complementary approaches can be used: the full calibration of the robot (all extrinsic and intrinsic parameters identified) and a partial calibration where only the extrinsic parameters are re-identified. These two approaches demonstrated that extrinsic parameters change the most with time/drift and then their re-identification enable to reach again a very high positioning accuracy. Combining these two approaches, it is possible to hold a high level of performances over long periods, typically a week, which appears particularly promising for a wide scope of applications and more especially at the micro and nano scales.

Acknowledgment

These works have been funded by the Franche-Comté region, the EUR EIPHI Graduate School (ANR-17-EURE-0002), ANR CEPAGE (ANR-16-CE24-0024) and by the French RENATECH network through its FEMTO-ST technological facility.

References

[1] S. Liu, Y.-F. Li, and D. Xing, "Sensing and control for simultaneous precision peg-in-hole assembly of multiple objects," *IEEE Transactions on Automation Science and Engineering*, 2019.
[2] O. Benson, "Assembly of hybrid photonic architectures from nanophotonic constituents," *Nature*, vol. 480, no. 7376, p. 193, 2011.
[3] D. Xing, F. Liu, S. Liu, and D. Xu, "Efficient insertion of partially flexible objects in precision assembly," *IEEE Transactions on Automation Science and Engineering*, vol. 16, no. 2, pp. 706–715, 2018.
[4] X. Fu, Y. Liu, and Z. Wang, "Active learning-based grasp for accurate industrial manipulation," *IEEE Transactions on Automation Science and Engineering*, vol. 16, no. 4, pp. 1610–1618, 2019.
[5] B. Komati, K. Rabenorosoa, C. Clévy, and P. Lutz, "Automated guiding task of a flexible micropart using a two-sensing-finger microgripper," *IEEE Transactions on Automation Science and Engineering*, vol. 10, no. 3, pp. 515–524, 2013.
[6] Y. Wen, H. Lu, Y. Shen, and H. Xie, "Nanorobotic manipulation system for 360° characterization atomic force microscopy," *IEEE Transactions on Industrial Electronics*, vol. 67, no. 4, pp. 2916–2924, 2019.
[7] J. Li, X. Li, T. Luo, R. Wang, C. Liu, S. Chen, D. Li, J. Yue, S.-h. Cheng, and D. Sun, "Development of a magnetic microrobot for carrying and delivering targeted cells," *Science Robotics*, vol. 3, no. 19, 2018.
[8] Y. Wei and Q. Xu, "A survey of force-assisted robotic cell microinjection technologies," *IEEE Transactions on Automation Science and Engineering*, vol. 16, no. 2, pp. 931–945, 2018.
[9] S. Yao, H. Li, K. Wang, and X. Zhang, "High-accuracy calibration of a visual motion measurement system for planar 3-dof robots using gaussian process," *IEEE Sensors Journal*, 2019.
[10] N. Tan, C. Clévy, and N. Chaillet, "Calibration of nanopositioning stages," *Micromachines*, vol. 6, no. 12, pp. 1856–1875, 2015.
[11] Ö, "Camera-robot calibration for the da vinci robotic surgery system."
[12] N. Tan, C. Clévy, G. J. Laurent, P. Sandoz, and N. Chaillet, "Accuracy quantification and improvement of serial micropositioning robots for in-plane motions," *IEEE Transactions on robotics*, vol. 31, no. 6, pp. 1497–1507, 2015.
[13] A. Nubiola, M. Slamani, A. Joubair, and I. A. Bonev, "Comparison of two calibration methods for a small industrial robot based on an optical cmm and a laser tracker," *Robotica*, vol. 32, no. 3, pp. 447–466, 2014.
[14] A. N. Andre, P. Sandoz, B. Mauze, M. Jacquot, and G. J. Laurent, "Sensing one nanometer over ten centimeters: A micro-encoded target for visual in-plane position measurement," *IEEE/ASME Transactions on Mechatronics*, 2020.
[15] C. Clévy, M. Rakotondrabe, and N. Chaillet, *Signal measurement and estimation techniques for micro and nanotechnology*. Springer Science & Business Media, 2011.

[16] T. S. Lembono, F. Suárez-Ruiz, and Q.-C. Pham, "Scalar: Simultaneous calibration of 2-d laser and robot kinematic parameters using planarity and distance constraints," *IEEE Transactions on Automation Science and Engineering*, vol. 16, no. 4, pp. 1971–1979, 2019.

[17] R. Wang, A. Wu, X. Chen, and J. Wang, "A point and distance constraint based 6r robot calibration method through machine vision," *Robotics and Computer-Integrated Manufacturing*, vol. 65, p. 101959, 2020.

[18] V. Guelpa, A. V. Kudryavtsev, N. L.-F. Piat, and S. Dembélé, "Accurate 3d-positioning in a sem through robot calibration," in *IEEE International Conference on Manipulation, Automation and Robotics at Small Scales*, pp 1–6, 2018.

[19] S. Liao, Q. Zeng, K. F. Ehmann, and J. Cao, "Parameter identification and non-parametric calibration of the tri-pyramid robot," *IEEE/ASME Transactions on Mechatronics*, 2020.

[20] Z. Xie, P. Zong, P. Yao, and P. Ren, "Calibration of 6-dof industrial robots based on line structured light," *Optik*, vol. 183, pp. 1166–1178, 2019.

[21] J. Zhang, X. Wang, K. Wen, Y. Zhou, Y. Yue, and J. Yang, "A simple and rapid calibration methodology for industrial robot based on geometric constraint and two-step error," *Industrial Robot: An International Journal*, 2018.

[22] Y.-J. Ren, J.-G. Zhu, X.-Y. Yang, and S.-H. Ye, "Measurement robot calibration model and algorithm based on distance accuracy," *Acta Metrologica Sinica*, vol. 3, p. 002, 2008.

[23] W. Zhenhua, X. Hui, C. Guodong, S. Rongchuan, and L. Sun, "A distance error based industrial robot kinematic calibration method," *Industrial Robot: An International Journal*, vol. 41, no. 5, pp. 439–446, 2014.

[24] M. R. Driels, W. Swayze, and S. Potter, "Full-pose calibration of a robot manipulator using a coordinate-measuring machine," *The International Journal of Advanced Manufacturing Technology*, vol. 8, no. 1, pp. 34–41, 1993.

[25] I. A. Sultan and J. G. Wager, "Simplified theodolite calibration for robot metrology," *Advanced Robotics*, vol. 16, no. 7, pp. 653–671, 2002.

[26] F. Li, Q. Zeng, K. F. Ehmann, J. Cao, and T. Li, "A calibration method for overconstrained spatial translational parallel manipulators," *Robotics and Computer-Integrated Manufacturing*, vol. 57, pp. 241–254, 2019.

[27] H. Bettahar, A. Caspar, C. Clévy, N. Courjal, and P. Lutz, "Photo-robotic positioning for integrated optics," *IEEE Robotics and Automation Letters*, vol. 2, no. 1, pp. 217–222, 2016.

[28] H. Bettahar, O. Lehmann, C. Clévy, N. Courjal, and P. Lutz, "Photo-robotic extrinsic parameters calibration of 6-dof robot for high positioning accuracy," *IEEE/ASME Transactions on Mechatronics*, pp. 1–1, 2020.

[29] P. Hariharan, *Basics of interferometry*. Elsevier, 2010.

[30] W. Khalil and J. Kleinfinger, "A new geometric notation for open and closed-loop robots," in *IEEE International Conference on Robotics and Automation. Proceedings*, vol. 3, 1986, pp. 1174–1179.

[31] S. Hayati and M. Mirmirani, "Improving the absolute positioning accuracy of robot manipulators," *Journal of Robotic Systems*, vol. 2, no. 4, pp. 397–413, 1985.

[32] W. Khalil and E. Dombre, *Modeling, identification and control of robots*. Butterworth-Heinemann, 2004.

Houari Bettahar received the graduate degree in Electrical and Electronic Engineering from the Institut de Génie Électrique et Électronique (IGEE), Boumerdes, Algérie in 2011. He received his Master degree in control system and information technology in 2014 from the University of Grenoble, France and his Ph. D. degree in Automatic Control and Robotics in 2019 from the University of Bourgogne-Franche-Comté , Besançon, France. Since 2018, he has been an teaching and research Officer at the University of Franche-Comté, Besançon, France working in the AS2M (Automatic Control and MicroMechatronic Systems) department of FEMTO-ST Institute. His research interests are the control of microrobotic and micro-assembly systems oriented to integrated optics.

Olivier Lehmann received the Engineer degree (M.S. degree) in automation, mechanics and computer sciences from ENSMM, Besançon, France, in 2000. He was an engineer in charge of technology transfer at the Institut de Productique and then at the Institut Pierre Vernier. In this context, he developed numerous robotics solutions dedicated to SMEs for 13 years and helped SMEs in their development. He is currently research engineer at FEMTO-ST. He is in charge of the development of several micro-nanorobotic stations in vacuum or non-vacuum environment. His scientific fields are robotics, control, vision and the development of integrated solutions.

Cédric Clévy received his Ph. D. degree in Automatic Control and computer Sciences in 2005 from the University of Franche-Comté, France. Since 2006, he has been an Associate Professor at the University of Bourgogne Franche-Comté, Besançon, France working in the AS2M (Automatic Control and MicroMechatronic Systems) department of FEMTO-ST Institute. His research interests are the design, modeling and control of micro and nanorobotic systems for the characterisation, manipulation and assembly at micro and nanoscales. Cédric Clévy currently leads the "Micro and Nano Robotics" research team of the FEMTO-ST Institute and co-leads the thematic research group "multiscale manipulation" of the Robotics Group of Research from the CNRS - National Research Center. He is also an active member of the IEEE/RAS technical committee for "Micro/Nano Robotics and Automation" and currently serving as Associate Editor for IEEE T-ASE and Technical Editor for IEEE/ASME T-Mech.

Nadège Courjal received her PhD degrees in "Engineering science" in 2002 and she has been Associate Professor at the FEMTO-ST Institute in Besançon since 2004. Her field of expertise relies on integrated optics and photonics, and most particularly electro-optic materials and lithium niobate. She also works on high resolution characterization of photonic components and nanostructures. Amongst her R&D activities in integrated optics and photonics, she has worked on the production of electro-optic sensors with Kapteos, chipscale spectrometers with Resolution Spectra, and low-chirp Mach-Zehnder Intensity modulators with iXBlue PSD. In the framework of academic research, she has had 3 DGA REI, RAPID & Astrid projects, and she is or has been the leader of 11 national projects, supported by ANR, BPI, Franche-Comté Region or SATT; she was also the project leader of one ActPhast project in 2016.

Philippe Lutz is Professor at the University of Franche-Comté, Besançon, since 2002. He was the head of the research group "Automated Systems for Micromanipulation and Micro-assembly" of the AS2M department of FEMTO-ST Institute from 2005 to 2011. He was the Director of the PhD graduate school of Engineering science and Microsystems with more than 400 PhD students from 2011 to February 2017, and he is currently the head of the Doctoral College. Since January 2017, he is the director of the AS2M Research department of FEMTO-ST. His research activities at FEMTO-ST are focused on the design and control of micro-nano systems, microgrippers, micro-nano robots, feeding systems and micro-nano manipulation, assembly stations, and Optimal design and control of piezoelectrically actuated compliant structures. P. Lutz received several awards of IEEE, authored over 90 refereed publications (50 in high standard journals), serves as associate editor for the IEEE T-ASE and as Technical Editor for the IEEE/ASME T-Mech, is member of several steering committees and is member of the IEEE Robotics and Automation Society (RAS) Committee on Micro-Nano Robotics.